Corresponding Author: Dr. Yidong Cai, Ph.D

Corresponding Author's Institution: China University of Geosciences, Beijing

First Author: Jin Cui

Order of Authors: Jin Cui; Dameng Liu; Yidong Cai, Ph.D; Zhejun Pan; Yingfang Zhou

Abstract: Fractures are the main pathways for fluid transport, which constrain the coalbed methane (CBM) reservoir permeability. Permeability is one of the key petrophysical parameters for CBM production. The fractures in the low and middle rank coals usually filled with minerals, which can significantly reduce the reservoir permeability. In this study, X-ray μ-CT combined with field emission scanning electron microscopy (FESEM) together with energy dispersive spectrometry (EDS) were used to quantitatively evaluate the features of fractures and minerals of FK sample (Ro,max 0.65%) and ML sample (Ro,max 1.49%) including morphology, complexity, volume and 3D structure, and its impacts on permeability. The results showed that fractures are well developed as observed in the samples FK and ML by the 2D cross section of X-ray μ-CT. Dolomite and kaolinite are common in the samples FK and ML as confirmed by FESEM images with EDS. Moreover, the 3D fracture structure including the open fracture and mineral filled fracture were reconstructed. The quantitative structural parameters (e.g. length, width, area and volume) of the fractures for these two samples were acquired by the commercial software Avizo 9.0.1. The middle rank coal of sample ML has larger fracture density (181 fractures per mm3) than that of the low rank coal of sample FK (104 fractures per mm3). Based on the reconstructured 2D and 3D fracture structure, the fracture complexity was evaluated through fractal dimension. And the impacts of mineralization in coals on petrophysical properties were evaluated, which show that the connectivity of fractures, porosity and permeability were greatly improved after demineralization. Therefore, this study may have implications for enhancing CBM recovery through demineralization.

Highlights

• Fractures and minerals of two Chinese coals were reconstructed by X-ray μ-CT.

• The open and mineralized fractures were quantitatively analyzed.

• Discrepancy of fractures and minerals in medium and low rank coals was evaluated.

• The importance of demineralization to enhance CBM production was illustrated.

Insights into fractures and minerals in subbituminous and bituminous coals by FESEM-EDS and X-ray μ-CT

Jin Cui[a,b], Dameng Liu[a,b], Yidong Cai[a,b*], Zhejun Pan[c], Yingfang Zhou[d]

[a] *School of Energy Resources, China University of Geosciences, Beijing 100083, China*

[b] *Coal Reservoir Laboratory of National Engineering Research Center of CBM Development & Utilization, China University of Geosciences, Beijing 100083, China*

[c] *CSIRO Earth Science and Resource Engineering, Private Bag 10, Clayton South, Victoria 3169, Australia*

[d] *School of Engineering, Fraser Noble Building, King's College, University of Aberdeen, AB24 3UE Aberdeen, UK*

Abstract: Fractures are the main pathways for fluid transport, which constrain the coalbed methane (CBM) reservoir permeability. Permeability is one of the key petrophysical parameters for CBM production. The fractures in the low and middle rank coals usually filled with minerals, which can significantly reduce the reservoir permeability. In this study, X-ray μ-CT combined with field emission scanning electron microscopy (FESEM) together with energy dispersive spectrometry (EDS) were used to quantitatively evaluate the features of fractures and minerals of FK sample ($R_{o,max}$ 0.65%) and ML sample ($R_{o,max}$ 1.49%) including morphology, complexity, volume and 3D structure, and its impacts on permeability. The results showed that fractures are well developed as observed in the samples FK and ML by the 2D cross section of X-ray μ-CT. Dolomite and kaolinite are common in the samples FK and ML as confirmed by FESEM images with EDS. Moreover, the 3D fracture structure including the open fracture and mineral filled fracture were reconstructed. The quantitative structural parameters (e.g. length, width, area and volume) of the fractures for these two

23 samples were acquired by the commercial software Avizo 9.0.1. The middle rank coal of

24 sample ML has larger fracture density (181 fractures per mm^3) than that of the low rank coal

25 of sample FK (104 fractures per mm^3). Based on the reconstructed 2D and 3D fracture

26 structure, the fracture complexity was evaluated through fractal dimension. And the impacts

27 of mineralization in coals on petrophysical properties were evaluated, which show that the

28 connectivity of fractures, porosity and permeability were greatly improved after

29 demineralization. Therefore, this study may have implications for enhanced CBM recovery

30 through demineralization.

32

1. Introduction

34 Coalbed methane (CBM) is a form of unconventional natural gas extracted from coal

35 reservoirs. In the past few decades, CBM has become a substantial source of clean energy, of

36 which the exploration and development have been successfully carried out in many countries

37 such as US, Australia, and Canada [1]. China has rich coal resources and abundant CBM

38 resources. The CBM exploration and development in China has been developing rapidly in

39 recent years. Statistically, the CBM resources below the depth of 2000 meters reach

40 $36.81 \times 10^{12} \, m^3$ and over 16000 CBM wells including vertical and horizontal wells were drilled

41 in China with an annual CBM output of $70.2 \times 10^8 m^3$ [2].

42 During the process of CBM production, gas flows through the fractures to the wellbore in

43 response to the pressure gradient [3]. When the reservoir pressure drops below the critical

44 CH_4 desorption pressure, the adsorbed CH_4 gradually diffuses from the micropores in coal

45   matrix to the macropores or fractures [4, 5] Therefore, the fractures are the main pathways for

46   gas and water flow. Normally the in-situ fractures were filling with minerals, which have

47   significant impacts on the fracture properties, and thus on fracture permeability. For instances,

48   minerals that include inherent or extraneous minerals (e.g. quartz, clay minerals, feldspars,

49   carbonates, and sulphide minerals) are often developed in the coal fractures [2]. The inherent

50   or extraneous minerals present differently in coals. Inherent minerals are normally syngenetic,

51   which are generally enclosed by or embraced in coal matrix, while extraneous mineral are

52   filling in fractures [3]. Therefore, the extraneous minerals can substantially reduce the

53   reservoir permeability and affects the process of gas production [4, 5]. The fracture

54   morphology, connectivity and density can be system acquired with multiple techniques (e.g.

55   optical microscope, AFM, FESEM, CT and NMRI) [5-7]. CT as a non-destructive technique

56   has been widely used to investigate the 3D structure of coals, which can obtain the specific

57   fracture parameters including fracture length and surface area [8]. Although the X-ray μ-CT

58   can distinguish the fractures, minerals and coal matrix, the specific minerals (e.g. quartz and

59   feldspars,) cannot be detected [9, 10]. In this study, an X-ray μ-CT combined with field

60   emission scanning electron microscopy and energy dispersive spectrometry will be adopted to

61   acquire the 3D structure information of fractures and minerals in coals.

62   Fracture complexity and irregularity can be described with the fractal geometry [11-14].

63   Fractal dimension (D) is an important characteristic parameter of fractal geometry, which can

64   quantitatively reflect the fracture complex in coals. Therefore, the fractal dimension may

65   indicate the CBM adsorption and flow capabilities [15]. The fractal dimension of fractures in

66   coals can be acquired by scanning electron microscopy (SEM), nuclear magnetic resonance

3

67 (NMR), mercury intrusion porosimetry and low-temperature N_2 adsorption/desorption

68 isotherm [16-18]. The X-ray μ-CT scanning can capture the detailed fracture structure in both

69 2D slices and 3D reconstruction patterns.

70 In this study, X-ray μ-CT together with FESEM-EDS scanning will be used to accurately

71 characterize the multiscale characteristics of 2D and 3D fracture structure and minerals

72 performance in the low rank coal sample FK and medium rank coal sample ML. Herein, the

73 fractal dimension of fractures in 2D and 3D view will be calculated, and the original and

74 de-mineralized coals will be compared to evaluate the effects of mineralization on fracture

75 properties. Firstly, the morphology of fractures and minerals were identified in 2D

76 FESEM–EDS. Secondly, X-ray μ-CT scanning was combined to accurately characterize the

77 multiscale characteristics of 3D fractures and minerals. And the fracture complexity and

78 irregularity were described with the fractal geometry. Finally, the impacts of fractures and

79 minerals performance on petrophysical properties including porosity and permeability were

80 detail discussed. This study provided a possible way to enhance CBM recovery through

81 demineralization.

82 ## 2. Experiments and methods

83 2.1. Coal basic information

84 One subbituminous coal from Fukang (FK) colliery in the southern Junngar Basin and another

85 bituminous coal from Malan (ML) colliery in the northwest Qinshui Basin were collected,

86 which were drilled for cylindrical cores with 25mm in diameter and 50mm in length

87 approximately. With Leitz MPV-3 photometer microscope, maceral composition analysis and

88 the maximum vitrinite reflectance ($R_{o, max}$) were performed on polished slabs as previous

89   research [7]. The proximate analysis was conducted on the Automatic Proximate Analyzer

90   5E-6600. The results as listed in Table 1 indicated that FK sample was a subbituminous coal

91   with $R_{o, max}$ of 0.65% that belong to low rank coal and the ML sample was a bituminous coal

92   with $R_{o, max}$ of 1.49% that belong to medium rank coal.

93   2.2. X-ray μ-CT scanning and FESEM-EDS

94   The CT measurements of the FK and ML samples were performed on the nanoVoxel-3502E

95   microfocus X-ray CT scan equipment. The cylindrical core samples (9.77mm in diameter and

96   15mm in length for sample FK, and 5.64mm in diameter and 10mm in length for sample ML)

97   was placed perpendicular to the sample couch, and was aligned in the center of the scanner

98   field of view. The X-ray source voltage and current were set to be 120KV, 36.67μA and

99   70KV, 40μA for the FK and ML samples, respectively. The CT equipment is able to produce

100   a voxel dataset containing a series of 2D slices with the resolution of 500 nm. The detector

101   has a resolution of 2048×2048 pixels, in which each pixel represents an area of

102   ~3.98×3.98um^2 for sample FK and 2×2um^2 for sample ML respectively. The spatial

103   resolution of sample FK and ML are approximately 3.98μm and 2μm, with which most

104   fractures can be distinguished.

105   Field emission scanning electron microscope (FESEM) with an energy dispersive

106   spectrometer and X-ray diffractometer were used to aid microfocus X-ray CT method and

107   recognize the mineral matter [19]. Coal samples were polished into lumps approximately 10

108   mm (length) ×10 mm (width) × 7 mm (height) with spluttered thin gold coating. The fractures

109   and mineral band in the range of 3nm-50μm can be measured using the FEI Quanta FEG 450

110   (FEI, America) and EDAX TEAM EDS.

111   2.3. 3D morphology reconstruction

112   For a typical CT grayscale image, each pixel corresponds to a grayscale that equals to specific

113   CT number. Normally, minerals with high CT number (approximately 3000 HU) present

114   white, whereas the fractures with low CT number (<600HU) show black, and coal matrix

115   with medium CT number (100-1600HU) correspond to a certain range of gray [8]. Then 3D

116   threshold segmentation (watershed segmentation), the process of partitioning of the greyscale

117   image into unique phases, was applied according to CT number. After that the partitions were

118   colored and the 3D model of each partition was established. The image data from the X-ray

119   μ-CT was imported into Avizo 9.0.1, the commercial software for 3D visualization,

120   reconstruction and analysis. The representative elemental volume (REV) under the subvolume

121   extraction is important due to the computational capability of the computers and the coal

122   strong heterogeneity [20]. The size of digital core REVs for sample FK and ML was

123   determined to be 2000 μm × 2000 μm × 2000 μm to assess the properties of organics,

124   fractures and minerals with thousand 2D slices stacked together.

125   2.4. Fractal dimension calculation of fractures

126   The fractals of fractures can be evaluated by box-counting dimension method, fractal Brown

127   motion method and area measurement method [21]. In this study, 2D and 3D box-counting

128   methods were employed to calculate the fractal dimension of 2D slices and reconstructed

129   REV. The box-counting method divides the image space or volume into square boxes of each

130   size δ. By decreasing the size of the square boxes by half, the number of square boxes

131   N(δ) contained fractures can be counted, which depends on the size of the square box [22]:

132    $N(\delta) \sim \delta^{-D}$ (1)

133   Then, a log-log plot composed of the number of the boxes $N(\delta)$ versus the different size of

134   boxes δ can be plotted. Finally, the linear fitting equation can be established below:

135    $\log(N(\delta)) = -D\log(\delta) + \log(\alpha)$ (2)

136   Where, $N(\delta)$ is the number of square boxes contained fractures, δ is the size of square

137   boxes, α is constant, and D is the fractal dimension of fractures.

138   2.5. Permeability evaluation

139   The absolute permeability simulation can be conducted through Avizo XLab Extension with a

140   finite volume method. The equations used in the absolute permeability simulation are

141   discretized on a staggered grid to allow a better estimation of the no-slip boundary condition.

142   Before absolute permeability simulation, the isolated fracture space should be removed and

143   extract the connected fracture space through Avizo software. The aim is to assure that the

144   fracture space existing in the samples allows fluid pass through. The definition of absolute

145   permeability is based on Darcy's law:

146    $\dfrac{Q}{S} = -\dfrac{k}{\mu}\dfrac{\Delta P}{L}$ (3)

147   Where Q is the flow rate (m^3 per second); S is the cross section area (m^2); k is the absolute

148   permeability (m^2); μ is the dynamic viscosity of the fluid (Pa·s); ΔP is the pressure difference

149   (Pa); L is the sample length in the flow direction (m).

150   To numerically estimate absolute permeability, the Stokes equations are solved:

151    $\begin{cases} \vec{\nabla}.\,\vec{V} = 0 \\ \mu\nabla^2\,\vec{V} - \vec{\nabla}P = \vec{0} \end{cases}$ (4)

152   Where $\vec{\nabla}.$ is the divergence operator; $\vec{\nabla}$ is the gradient operator; $\vec{V}$ is the velocity of the

153   fluid in the fluid phase of the material; μ is the dynamic viscosity of the flowing fluid; ∇^2 is

154   the Laplacian operator; P is the pressure of the fluid in the fluid phase of the material. This

155 simplified Navier-Stokes equations considering an incompressible fluid means the density is a

156 constant; A Newtonian fluid means the dynamic viscosity is a constant; A steady-state flow

157 means the velocity does not vary over time; A laminar flow means the concerned velocities

158 are small enough not to produce turbulence. The simulated flow direction can be adjusted to

159 X, Y or Z direction respectively. The inflow pressure was set to be 1.3×10^5 Pa, the outflow

160 pressure was set to be the atmospheric pressure, and the water viscosity is 1.005×10^{-3} Pa·s.

3. Results and discussion

162 3.1. 2D morphology of fractures

163 Fig. 1 shows the typical 2D morphology of fractures obtained by X-ray μ-CT, which can be

164 divided into two categories: syngenetic fractures (also named cleats) that formed during the

165 process of coalification, and exogenous fractures that formed during deformation and faulting

166 by tectonic movements [23]. The cleats commonly occur in orthogonal fractures, face cleats

167 and butt cleats (a1-2, b1-2 in Fig. 1) [24]. Face cleats formed first during coalification, and

168 butt cleats formed later and terminated by face cleats [25]. Face cleats were dominant and

169 extensive, which were wider than butt cleats [26]. The face cleats were basically filled with

170 minerals, whereas no mineralization was observed in butt cleat (a1-2, b1-2 in Fig. 1).

171 Cleat-filling minerals were epigenetic, which mainly precipitate along the face cleats from the

172 solutions with various compositions and temperatures [27].

173 With the aid of energy dispersive spectrometer, the main fracture filling minerals of sample

174 FK and ML are identified as dolomite (a3 and a4 in Fig. 1) and kaolinite (b3 and b4 in Fig. 1),

175 which indicates that the minerals were deposited by the movement of mineralized fluid

176 through the coal seam after the development of major fractures. Gypsum are widely spread in

the coal matrix as inherent minerals in the sample FK, and calcite and pyrite occurs as

individual grains in coal matrix of the sample ML. Mineral in threshold segmentation can be

divided into two categories: fracture-filling minerals and scattered minerals in both sample

FK and ML. FESEM imaging (a3 and b3 in Fig. 1) shows the width of open fractures in

sample FK and ML are in the range of 0.59-1.83μm and 1.335-12.6μm, while mineralized

fractures are in the range of 6.07-40.56μm and 0.13-66.85μm respectively. The width of

mineral-filling fracture varies greatly compared with the open fractures and mineralized fluids

mainly flow in large fractures with the width greater than 10μm.

3.2. 3D reconstructed fractures

3D fracture reconstructed structures were established by 2D X-ray μ-CT slices to determine

the fracture networks. A1 and b1 in Fig. 2 shows that the 3D reconstructed volumes of

original FK and ML coals were divided into coal matrix in black, fractures in blue and

minerals in yellow. A2 and b2 Fig. 2 shows the 3D structure of FK and ML coals after

grayscale threshold segmentation. Fractures are composed of unmineralized fractures in blue,

mineral filled fractures in pink. And scattered minerals within coal matrix are presented in

yellow. Herein, the mineral filled fractures are the same as fracture filled minerals due to the

same threshold segmentation. The volume fraction of each part was calculated through the

number of pixels (volume) by CT scanning. The volume fractions of scattered minerals for

the samples FK and ML are 0.55% and 13.98% respectively. The mineral-filled fractures or

fracture-filling minerals accounts for 10.77% and 7.46% for the samples FK and ML

respectively, which occupy 96.42% and 90.31% of the total fractures. Therefore, most

fractures in both sample FK and ML were filled with minerals and these fractures that filling

9

minerals may inhibit the fluid flow process due to the decrease in fracture width of the seepage path, which is unfavorable for CBM production, especially when the mineral filled fractures have wonderful connectivity (a2 and b2 in Fig. 2). Therefore, demineralization could be an effective way to increase the fluid flow path and the fractures connectivity, and thus possibly increase the permeability.

3.3. The evaluation of fractures complexity

3.3.1. Structure evaluation of fractures

The fracture density for sample FK was 839 fractures within the volume of 8 mm^3 (149 open fractures and 690 mineral-filling fractures per mm^3), whereas 1451 fractures per 8 mm^3 (1436 open fractures and 15 mineral-filling fractures per mm^3) for sample ML, which indicates that more fractures developed in sample ML than that of sample FK. During coalification ($R_{o, max}$<0.65%), the dehydration and volatiles loss will result in the formation of microfractures [28]. When $R_{o, max}$>1.30%, the fracture density will decrease slowly and then remain constant with increasing coal rank [29]. The structural parameters (average length, average width, average area and average volume) for open fractures, mineral-filling fractures and total fractures of the two samples were presented in Table 2 and Fig. 3. 3D visualization of open fracture and total fracture in different length scale were presented in Fig. 4. The average width and average volume in sample ML are reduced by 45.94% and 56.78% compared to sample FK and the other average structural parameters including fracture length, area decrease with increasing coal rank (low-rank to medium-rank). At the early coalification of $R_{o, max}$=0.6%-1.2%, overburden pressure results in structural parameters decreased with the increase of coal rank [30-32]. When $R_{o,max}$ is in 1.25%-2.25%, the small-molecule compounds

10

221 escape from the coal as gases (H_2O, CO_2, and CH_4) and the average structural parameters

222 continue to decrease because of the overburden pressure and matrix shrinkage, but the rate of

223 decline slows [33]. Mineral-filling fractures occupy 96.42% and 90.31% volume in total

224 fractures for samples FK and ML, which means most fractures are filled with minerals carried

225 by underground fluid. The average width of total fractures increased by 4.46% and 9.87%

226 compared to open fractures and the maximum fracture width changes from 35.95μm to

227 55.81μm and 19.11μm to 98.96μm for samples FK and ML respectively, which indicates that

228 the fluid flow space will be greatly improved if mineral-filling fractures are de-mineralized.

229 3.3.2. Fractures complexity by fractal dimension

230 Fractal method was used to evaluate the complexity of fractures [25]. Generally, the

231 microfractures become much more complex as coal rank increase, which leads to the high

232 fractal dimension [31]. The 2D and 3D fractal dimension of open and total fracture of FK

233 sample were calculated by box dimension method as shown in Fig. 5. The following size of

234 square or cube is used (in pixels): 4, 8, 16, 32 and 64. The calculation for obtaining 2D and

235 3D fractal dimension can be seen in Fig. 6. For 2D fractal dimension of fractures, 16 slices

236 were selected evenly to calculate the 2D fractal dimension for sample FK and ML

237 respectively. 2D fractal dimension of fractures varies from slice to slice due to the strong

238 heterogeneity. However, the 3D fractal dimension can represent the fracture complexity of the

239 whole sample. The average 2D and 3D fractal dimensions of open fractures in sample ML are

240 1.16 and 2.172 respectively, which are lower than those of sample FK (1.25, 2.242). Whereas

241 the average value of total fractures for sample ML are 1.50 and 2.519, which are higher than

242 those of sample FK (1.44, 2.403) after demineralization. Therefore, the fractal dimension of

243   fractures in de-mineralized samples, whether 2D or 3D fractal dimensions, increased greatly

244   compared with original open fractures, which means that the value of fractal dimension

245   increases with the degree of fracture development. The 2D and 3D fractal dimension of

246   original open fractures in sample ML are lower than those of sample FK. However, both 2D

247   and 3D fractal dimension of total fractures in sample ML exceed those in sample FK after

248   demineralization for mineral-filling fractures. Therefore, the mineralization of sample ML is

249   more serious.

250   3.4. Insights into petrophysical properties of coals

251   3.4.1 Fracture porosity

252   The fracture porosity of the original open and de-mineralized fractures was numerically

253   calculated to evaluate the effect of minerals on permeability. The fracture porosity of samples

254   FK and ML were obtained from micro-CT data as shown in Fig. 7. For original open fractures,

255   the open fracture porosity in different directions has an average difference of 2.1%, while the

256   total fracture porosity included de-mineralized fractures shows variable porosity with an

257   average difference of 6.3% in different directions, which indicate that the fracture has strong

258   heterogeneity in different directions. The fracture porosity varies from slice to slice. For

259   sample FK and ML, the average total fracture porosity of the de-mineralized samples are

260   6.85% and 11.47%, which increased by 6.39% and 10.37% compared with original open

261   fractures porosity. If the minerals-filling fractures are de-mineralized or acidified, these

262   fractures will be favorable for enhancing CBM recovery. Fig. 8 shows the correlation between

263   the fractal dimensions of fractures and CT fracture porosity. The CT porosity shows an

264   approximately U-shaped change with 2D fractal dimensions or 3D fractal dimensions, which

265   presents similar tendency: porosity firstly decreases from 1.1% to 0.46%, then increases with

266   fractal dimension increasing.

267   3.4.2. Fracture permeability

268   The fracture connectivity is another important factor influencing permeability in coals. Fig. 9

269   show the 3D spatial distribution of connected/unconnected fractures of original samples (a1

270   and b1 in Fig. 9) and de-mineralized samples (a2 and b2 in Fig. 9), respectively. The volume

271   fractions of connected fractures in open and total fractures for sample FK are 33% and 89%,

272   respectively. For sample ML, the volume fractions of the connected fracture are 54.1% and

273   98.4% in open and total fractures, respectively, which indicated that more than half of the

274   open fractures are isolated. And most mineral-filling fractures are well connected with other,

275   which will result in the favorable fluid flow path in fractures after mineral removed. The

276   connective fractures, as effective flow paths, can cause permeability increase for water/gases.

277   In this work, the absolute permeability simulation was conducted based on visualized

278   geometrical properties by micro-CT images [30]. The absolute permeability sharply increase

279   from 400 mD to 450 mD for sample FK and 0 mD to 740 mD for sample ML in the Y axis

280   after demineralization, and increase by 92% and 25% in Z axis after mineral removed, which

281   indicates that more connected fractures were provided for fluid flow. Therefore,

282   de-mineralization or acidification could be very important way for enhancing CBM

283   production. One thing that needs to clear is the result from numerical simulation varied

284   widely from laboratory result, which attribute to the significant interactions of gas, water and

285   fracture-wall that can significantly influence the permeability [31]. Pores that have been

286   neglected in the simulation also occur in coal, which also can make contribution to coal

287 permeability [34]. The difference of permeability indicates the importance of

288 de-mineralization of mineral filling fractures. Therefore, this fracture permeability simulation

289 with and without mineral filling can be conducive to enhancing CBM production.

4. Conclusions

291 X-ray μ-CT and field emission scanning electron microscope (FESEM) together with energy

292 spectrum experiment (EDS) can be used as effective means to evaluate fracture structure and

293 mineral performance in different rank coals (samples FK and ML). The structure, fracture

294 porosity, connectivity and permeability of open fracture and total fractures was quantitatively

295 evaluated by 2D and 3D fracture model and calculated to illustrate the effect of minerals on

296 flow capability. The following conclusions are made:

297 1) The well developed microfractures and dolomite and kaolinite filled microfractures present

298 in samples FK and ML, which were confirmed by FESEM images and 2D slices of X-ray

299 μ-CT together with EDS. The 3D reconstructed open fractures and total fractures of samples

300 FK and ML show the significantly changes in fracture structure.

301 2) The variable structure parameters (e.g. length, width) indicate that coal rank has significant

302 influence on fracture structure. The fracture density in medium rank coal (sample ML) is two

303 times than that in low rank coal (sample FK), while the structural parameters (average

304 fracture length, width, and volume) reduce as coal rank increase. The fracture structure

305 becomes more complex with the growth of fractal dimensions due to the matrix shrinkage and

306 overburden pressure during the coalification jump.

307 3) The permeability simulation reveals that the structural parameters (e.g. fracture porosity,

308 connectivity and permeability) of the fractures and the minerals have important impacts on

14

permeability. The volume of connected fractures and the porosity sharply increased after

mineral removal, which can significantly improve the permeability. Therefore,

demineralization or acidification can be used to increase the void space and connectivity of

the mineral-filling fractures, and will be favorable for enhancing CBM production.

Acknowledgements

References

[1]   Moore TA. Coalbed methane: A review. Int J Coal Geol 2012; 101(6):36-81.

[2]   Xu JZ, Zhai C, Liu SM, Wu SJ. Pore variation of three different metamorphic coals by

       multiple freezing-thawing cycles of liquid CO_2 injection for coalbed methane recovery. Fuel

       2017; 208:41-51.

[3]   Pan JN, Zhao YQ, Hou QL, Jin Y. Nanoscale pores in coal related to coal rank and

       deformation structures. Transport Porous Med 2015; 107(2):543-554.

[4]   Harvey RD, Ruch RR. Mineral matter in Illinois and other U.S. Coals. ACS Symposium,

       1986; 10-40.

[5]   Bryers RW. Influence of segregated mineral matter in coal on slagging. ACS Symposium

       Series. 1986; 353-374.

[6]   Gamson PD, Beamish BB, Johnson DP. Effect of coal microstructure and secondary

mineralization on methane recovery. Geological Society London Special Publications. 1996; 109(1):165-179.

[7] Cai YD, Liu DM, Pan ZJ, Yao YB, Li CC. Mineral occurrence and its impact on fracture generation in selected Qinshui Basin coals: An experimental perspective. Int J Coal Geol 2015; 150-151(4):35-50.

[8] Cnudde V, Boone MN. High-resolution X-ray computed tomography in geosciences: A review of the current technology and applications. Earth-Sci Rev 2013; 123(4):1-17.

[9] Geet MV, Swennen R, David P. Quantitative coal characterisation by means of microfocus X-ray computer tomography, colour image analysis and back-scattered scanning electron microscopy. Int J Coal Geol 2001; 46(1):11-25.

[10] Wang LB, Frost JD, Voyiadjis GZ, Harman TP. Quantification of damage parameters using X-ray tomography images. Mech Mater 2003; 35(8):777-790.

[11] Karacan CÖ, Okandan E. Fracture/cleat analysis of coals from Zonguldak Basin (northwestern Turkey) relative to the potential of coalbed methane production. Int J Coal Geol 2000; 44(2):109-125.

[12] Mazumder S, Wolf KHAA, Elewaut K, Ephraim R. Application of X-ray computed tomography for analyzing cleat spacing and cleat aperture in coal samples. Int J Coal Geol 2006; 68(3):205-222.

[13] Wang HM, Liu Y, Song YC, Zhao YC, Zhao JF, Wang DY. Fractal analysis and its impact factors on pore structure of artificial cores based on the images obtained using magnetic resonance imaging. J Appl Geophys 2012; 86(8):70-81.

[14] Mandelbrot BB. Statistical self-similarity and fractional. Science 1967; 156:636-638.

353   [15] Mahamud MM, Novo MF. The use of fractal analysis in the textural characterization of coals.

354   Fuel 2008; 87(2):222-231.

355   [16] Jörn H. Kruhl. Fractal-geometry techniques in the quantification of complex rock structures:

356   A special view on scaling regimes, inhomogeneity and anisotropy. J Struct Geol 2013;

357   46(46):2-21.

358   [17] Yao YB, Liu DM, Tang DZ, Tang SH, Huang WH, Liu ZH, Che Y. Fractal characterization of

359   seepage-pores of coals from China: An investigation on permeability of coals. Comput

360   Geosci 2009; 35(6):1159-1166.

361   [18] Zhou SD, Liu DM, Cai YD, Yao YB. Fractal characterization of pore–fracture in low-rank

362   coals using a low-field NMR relaxation method. Fuel 2016; 181:218-226.

363   [19] Cai YD, Liu DM, Pan ZJ, Che Y, Liu ZH. Investigating the effects of seepage-pores and

364   fractures on coal permeability by fractal analysis. Transport Porous Med 2016; 111(2): 1-19.

365   [20] Sun WJ, Feng Y Y, Jiang C F, Chu W. Fractal characterization and methane adsorption

366   features of coal particles taken from shallow and deep coalmine layers. Fuel 2015; 155:7-13.

367   [21] Bird MB, Butler SL, Hawkes CD, Kotzer T. Numerical modeling of fluid and electrical

368   currents through geometries based on synchrotron X-ray tomographic images of reservoir

369   rocks using Avizo and COMSOL. Comput Geosci 2014; 73:6-16.

370   [22] Mostaghimi P, Armstrong RT, Gerami A, Hu Y, Jing Y, Kamali F, Liu M, Liu ZS, Lu X,

371   RAmandi HL, Zamani A, Zhang YL. Cleat-scale characterisation of coal: An overview. J Nat

372   Gas Sci Eng 2017; 39:143-160.

373   [23] Alberichbayarri A, Martibonmati L, Angeles PM, Sanzrequena R, Lermagarrido JJ,

374   Garcíamartí G, Moratal D. Assessment of 2D and 3D fractal dimension measurements of

375   trabecular bone from high-spatial resolution magnetic resonance images at 3 T. Med Phys

376   2010; 37(9):4930-4937.

377   [24] Zhao YX, Zhu GP, Dong YH, Danesh NN, Chen ZW, Zhang T. Comparison of low-field

378   NMR and microfocus X-ray computed tomography in fractal characterization of pores in

379   artificial cores. Fuel 2017; 210:217-226.

380   [25] Niu QH. Micrometer-scale fractures in coal related to coal rank based on micro-CT scanning

381   and fractal theory. Fuel 2018; 212:162-172

382   [26] Laubach SE, Marrett RA, Olson JE, Scott AR. Characteristics and origins of coal cleat: A

383   review. Int J Coal Geol 1998; 35(1-4):175-207.

384   [27] Scholtès L, Donzé FV, Khanal M. Scale effects on strength of geomaterials, case study: Coal.

385   J Mech Phys Solids 2011; 59(5):1131-1146.

386   [28] Liu SQ, Sang SX, Wang G, Ma JS, Wang X, Wang WF, Du Y, Wang T. FIB-SEM and X-ray

387   CT characterization of interconnected pores in high-rank coal formed from regional

388   metamorphism. J Petrol Sci Eng 2017; 148:21-31

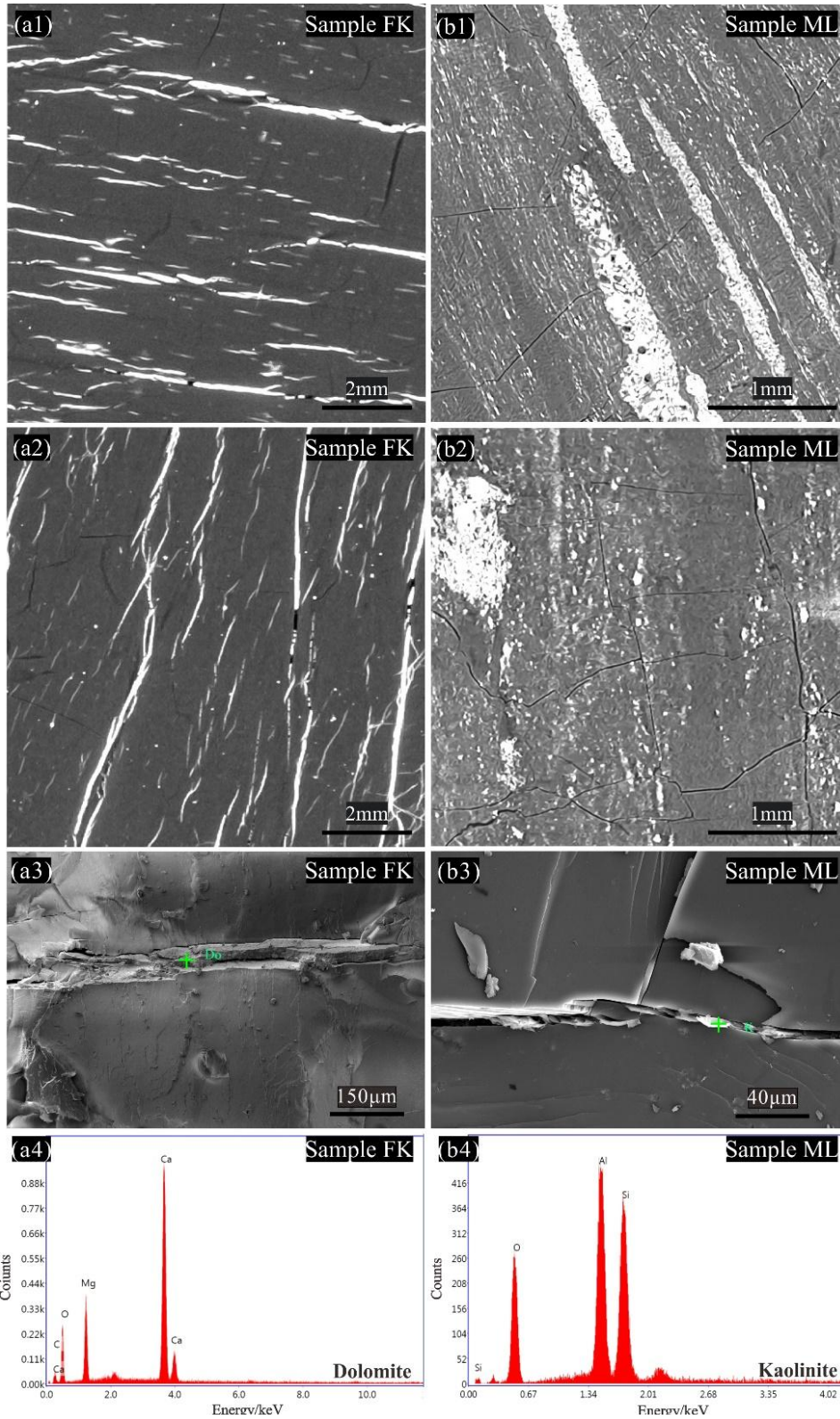389   [29] Wang ZZ, Pan JN, Hou QL, Yu BS, Li M, Niu QH. Anisotropic characteristics of low-rank

390   coal fractures in the Fukang mining area, China. Fuel 2018; 211:182-193.

391   [30] Yu J, Armstrong RT, Mostaghimi P. Digital coal: Generation of fractured cores with
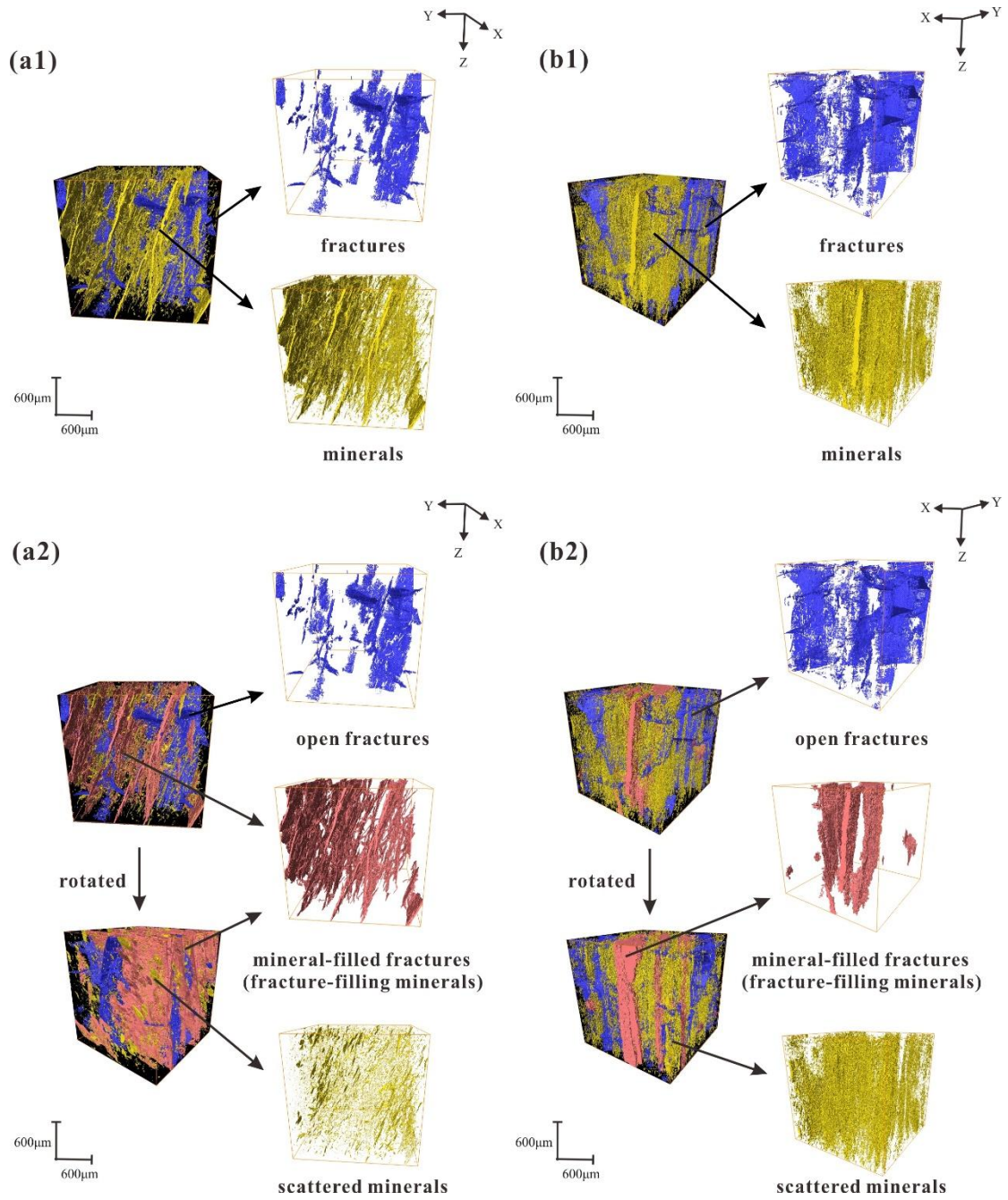
392   microscale features. Fuel 2017; 207:93-101.

393   [31] Abdelfatah E, Pournik M, Shiau BJB, Hrawell J. Digital coal: Generation of fractured cores

394   with microscale features. J Nat Gas Sci Eng 2017; 40:1-16.

395   [32] Kopp OC, Iii MEB, Clark CE. Volatiles lost during coalification. Int J Coal Geol 2000;

396   44(1):69-84.

397   [33] Su XB, Feng YL, Chen JF, Pan JN. The characteristics and origins of cleat in coal from

398   Western North China. Int J Coal Geol 2001; 47(1):51-62.

399   [34] Cai Y, Liu D, Yao Y, Li J, Qiu Y. Geological controls on prediction of coalbed methane of No.

400   3 coal seam in Southern Qinshui Basin, North China. Int J Coal Geol 2011; 88:101-112.

Fig.1 Typical 2D morphology of fractures obtained by X-ray μ-CT(a1, a2, b1,b2) and FESEM (a3,b3). X-y plane (a1,b1) and y-z plane (a2,b2) cross-section of sample FK and ML. Fractures in sample FK filled with dolomite (a3) and the spectrum obtained from a point on dolomite's surface (a4). Fractures in sample ML filled with kaolinite (b3) and the spectrum obtained from a point on dolomite's surface (b4).

Fig.2 3D visualization of original sample FK (a1) and ML (b1), re-segmented sample FK (a2) and sample ML (b2). For original samples (a1,b1), coal matrix are shown in black, fractures are shown in blue and minerals components are shown in yellow. For re-segmented samples (a2, b2), open fractures are shown in blue, mineral-filled fractures (fracture-filling minerals) are shown in pink, and scattered minerals are shown in yellow.
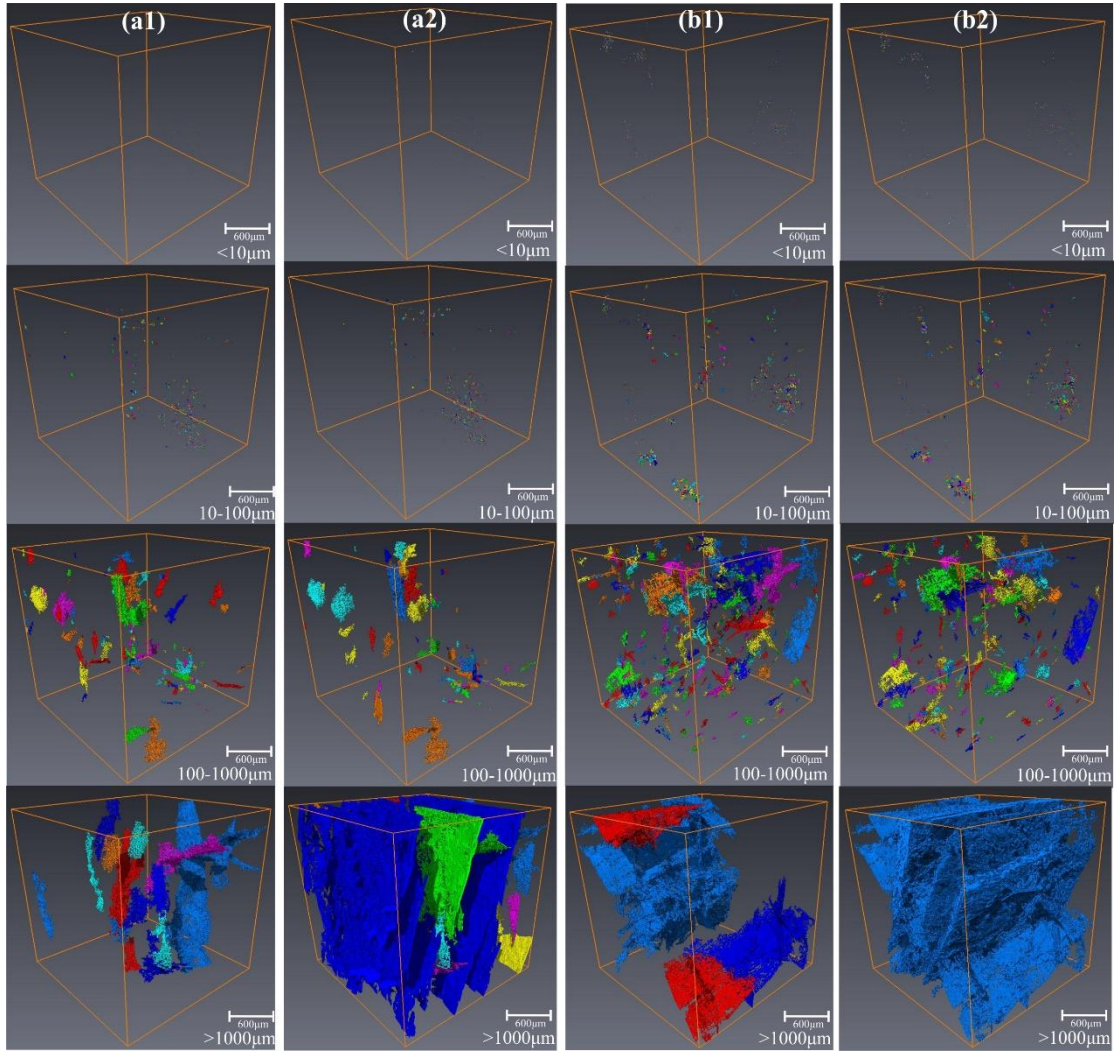
415

416

417
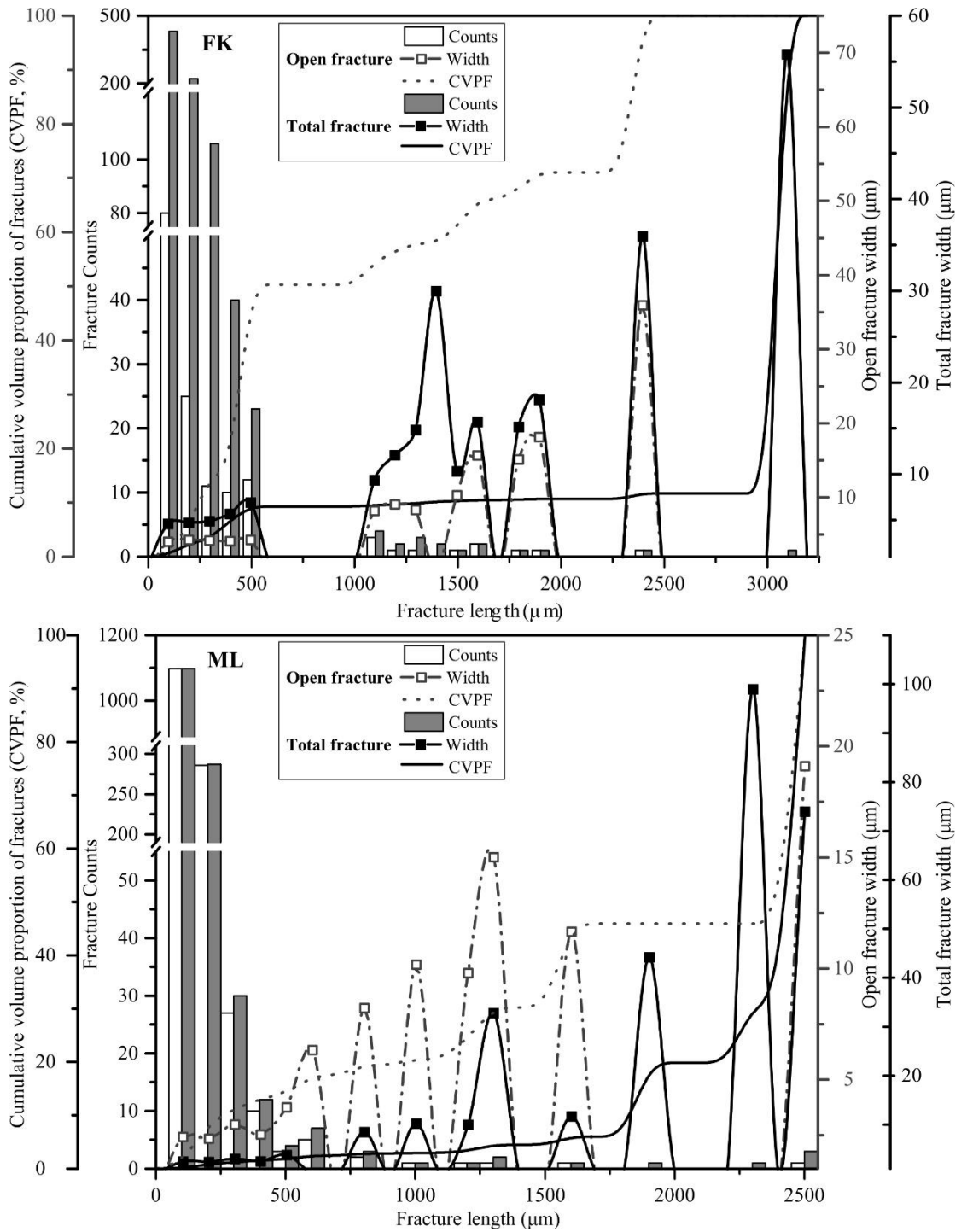
Fig.3 The counts, average width and cumulative volume proportion of open fracture and total fracture in different length scale.
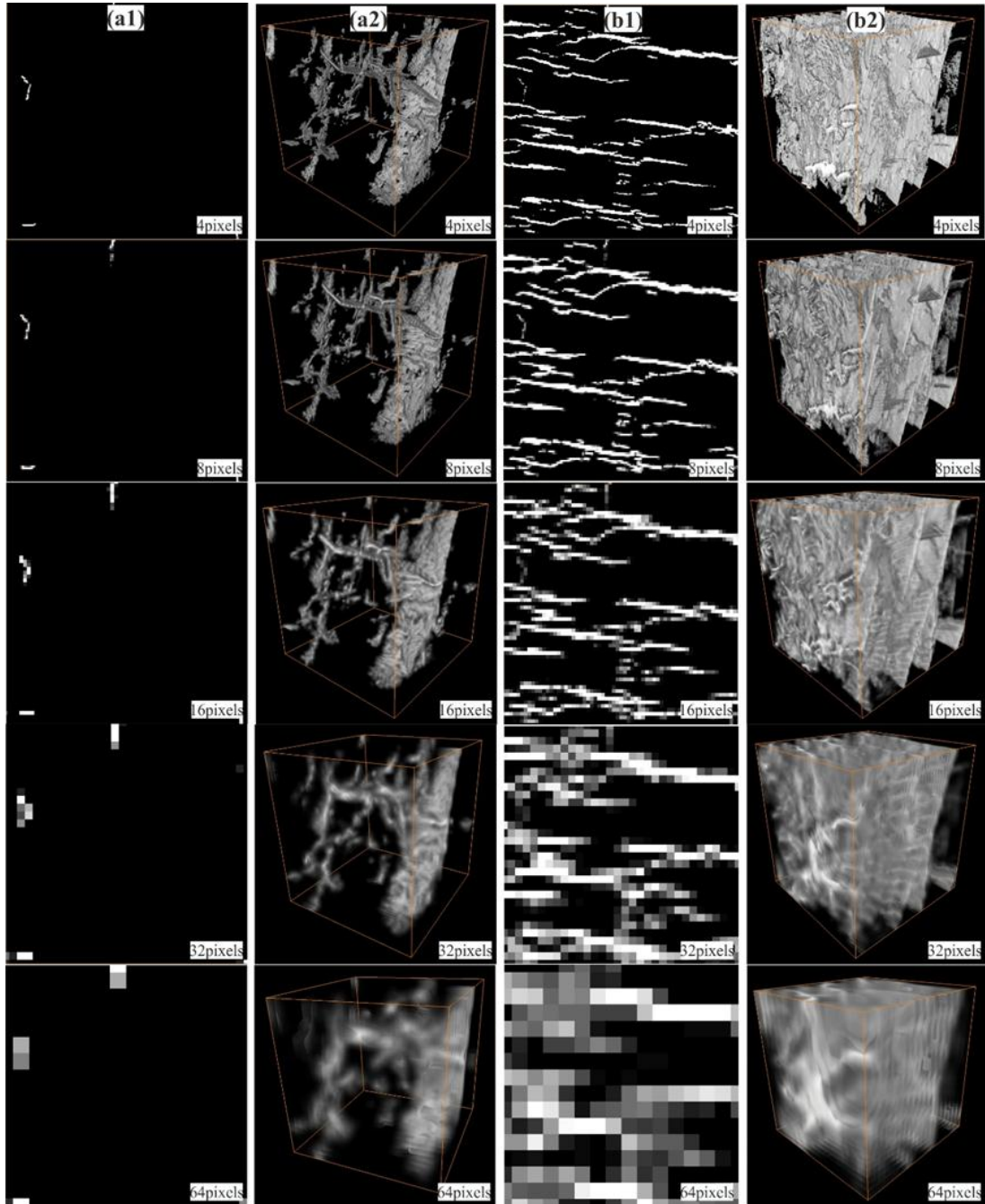
419

Fig.4 Different length scale of open fractures and total fractures in sample FK and ML: Fractures length<10μm, 10-100μm, 100-1000μm and >1000μm. (a1) Open fractures in sample FK; (a2) Total fractures in sample FK. (b1) Open fractures in sample ML. (b2) Total fractures in sample ML.

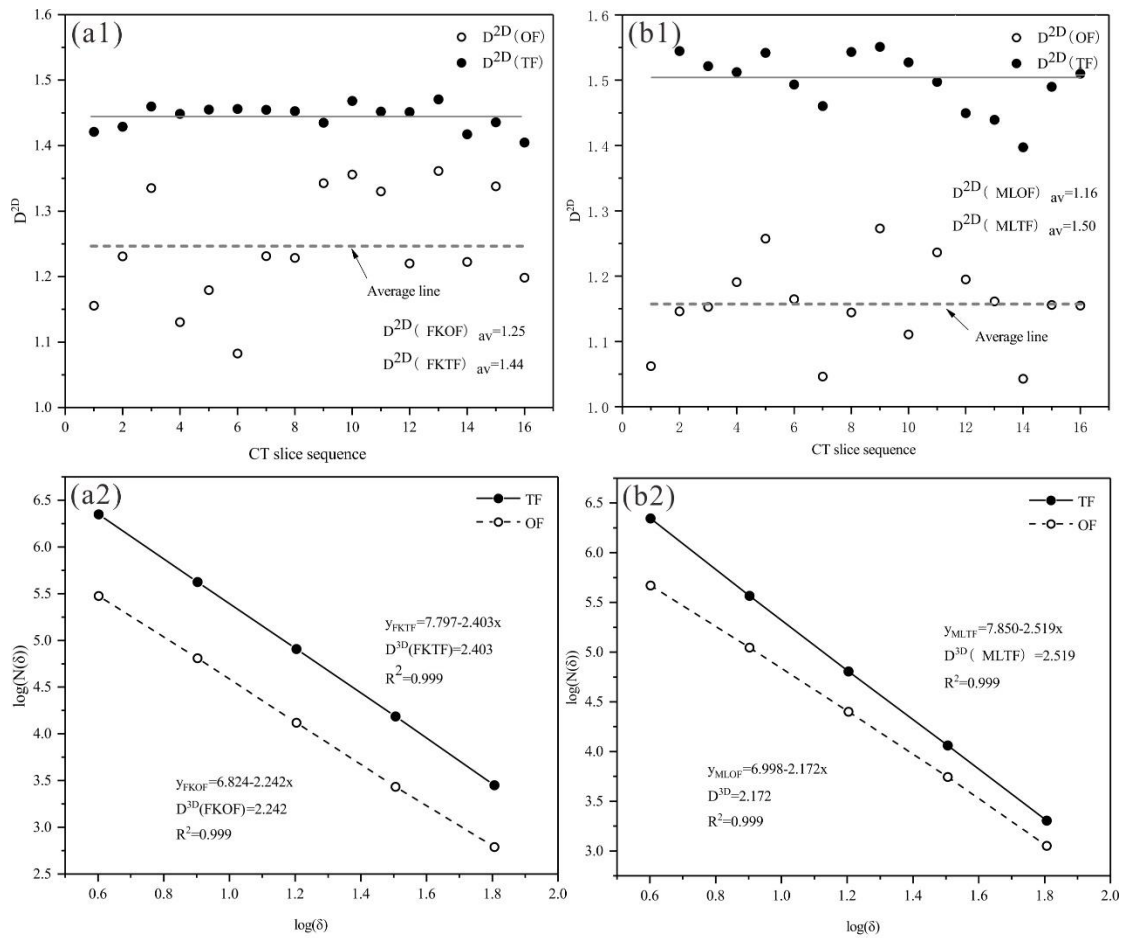Fig.5 Two dimension (2D) and three dimension (3D) fractal dimension calculation prosses of fracture in sample FK. (a1) 2D fractal dimension calculation prosses of open fracture, taking the 1st section along Z axis as example; (a2) 3D fractal dimension calculation prosses of open fracture in sample FK; (b1) 2D fractal dimension calculation prosses of total fracture, taking the 1st section along Z axis as example; (b2) 3D fractal dimension calculation prosses of total fracture in sample FK. The size of square or cube were used (in pixels):4,8,16,32,and 64,especively.

Fig.6 The results of two dimension(2D) and three dimension(3D) fractal dimension of samples FK and ML. (a1)The 2D fractal dimension of open and total fractures in sample FK along Z axis direction; (a2)The 3D dimension of open and total fractures in sample FK; (b1) The 2D fractal dimension of open and total fractures in sample ML along Z axis direction;(b2) The 3D dimension of open and total fractures in sample ML. Notes: OF: Open fracture; TF: Total fracture.

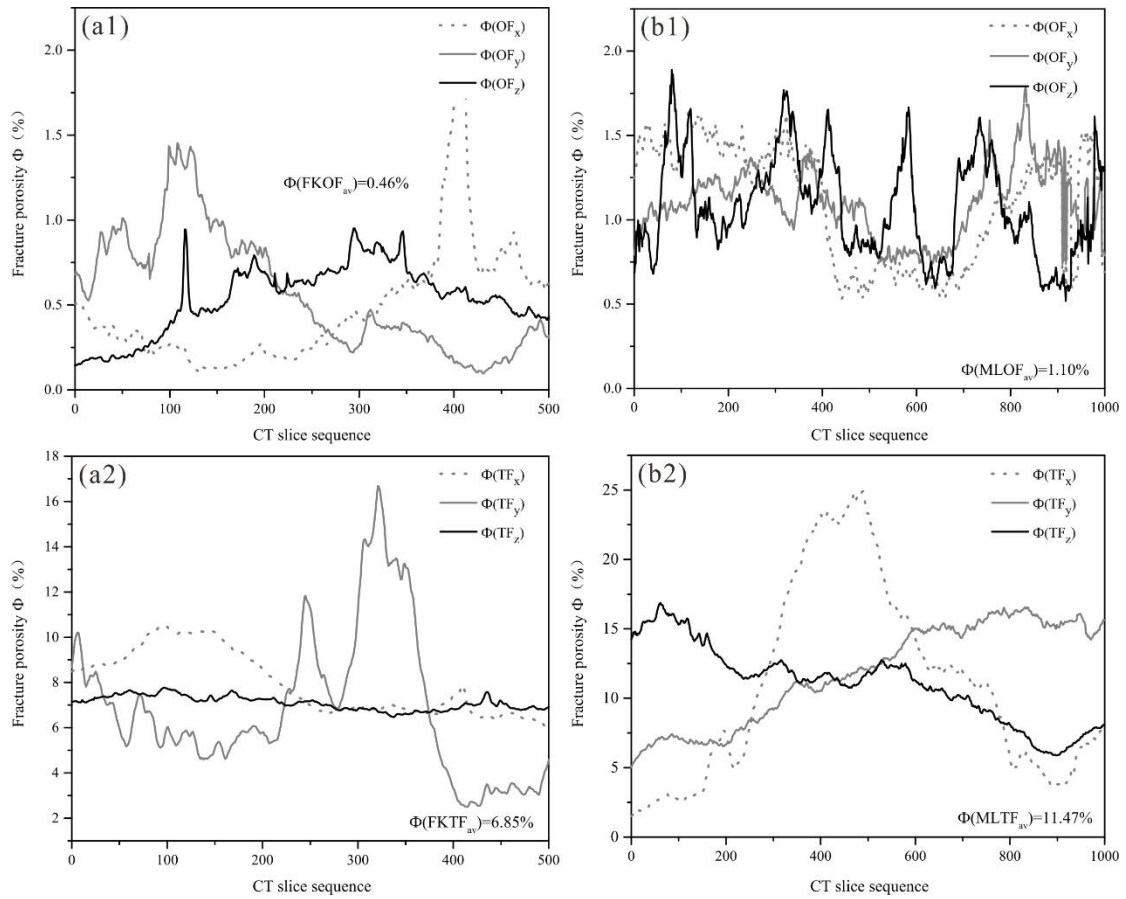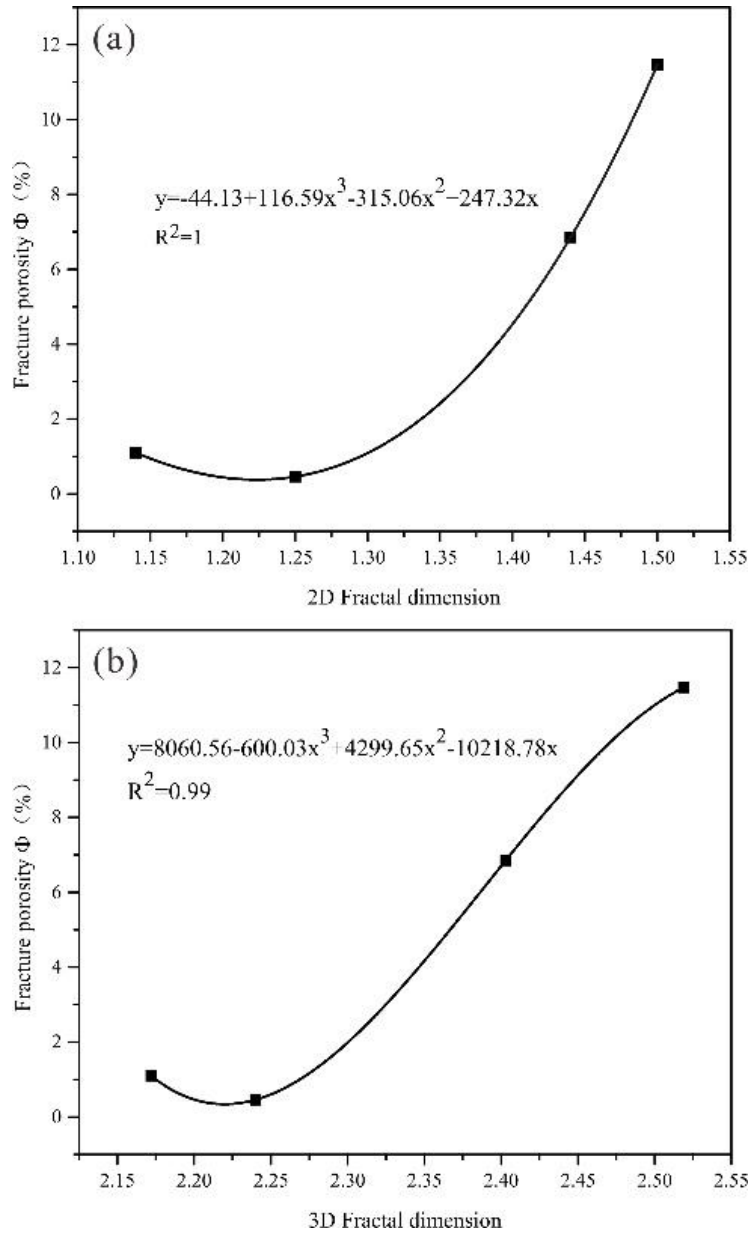Fig.7　Fracture porosity of original (Φ（OF）) and de-mineralized (Φ（TF）) of samples FK and ML in different directions. (a1) Fracture porosity of original sample FK (Φ（FKOF）); (a2) Fracture porosity of de-mineralized sample FK (Φ（FKTF）); (b1) Fracture porosity of original sample ML (Φ（MLOF）); (b2) Fracture porosity of de-mineralized sample ML (Φ（MLOF）). Notes: OF: Open fracture; TF: Total fracture.

452

453 Fig.8 The correlation between the fractal dimensions ((a):2D fractal dimension; (b)3D fractal dimension). Porosity firstly

454 decreases and then increases with fractal dimension increasing, displaying a 'U-shaped' trend.
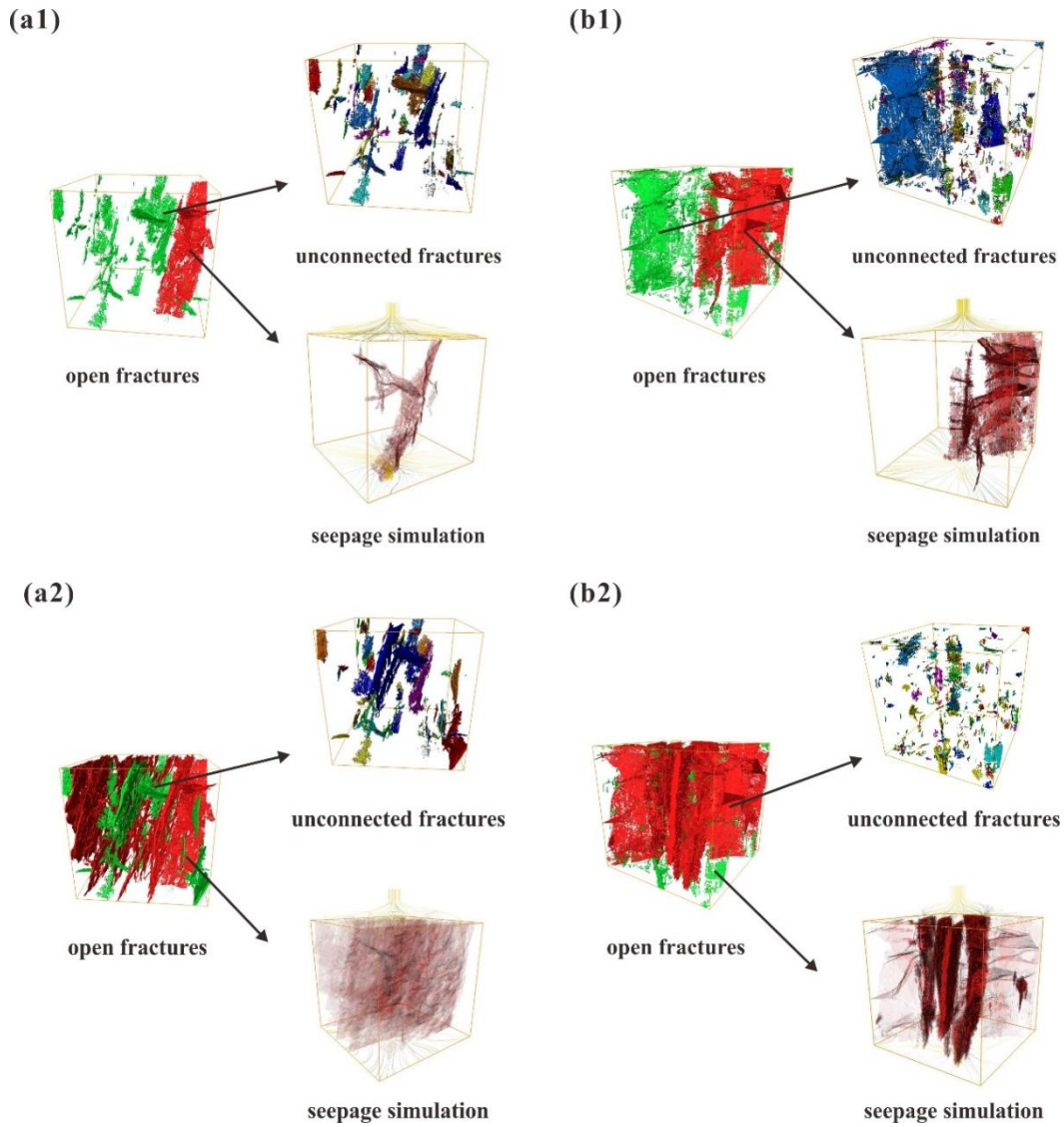
455

456

457

458

459

460

461

462

463

464

(a1)

unconnected fractures

open fractures

seepage simulation

(b1)

unconnected fractures

open fractures

seepage simulation

(a2)

unconnected fractures

open fractures

seepage simulation

(b2)

unconnected fractures

open fractures

seepage simulation

Fig.9 Results of connectivity analysis showing 3-D distribution of connected-unconnected fractures in original and de-mineralized sample FK (a1 and a2) and sample ML (b1 and b2). Further seepage simulation of connected fractures and 3-D distribution analysis of unconnected fractures were carried out. Connected fractures are shown in red and unconnected fractures are shown in green.

483   Table 1 Petrographic and proximate analysis results for two Chinese coals

Sample No.	$R_{o,max}$ (%)	Coal rank	Coal composition (Vol. %)			Proximate analysis (wt. %)			
			Vitrinite	Inertinite	Exinite	Mad	Aad	Vad	FCad
FK	0.65	subbituminous coal	83.9	1.7	14.5	3.76	8.86	39.21	48.17
ML	1.49	bituminous coal	67.6	32.4	0	0.29	9.97	14.73	75.01

484     $R_{o,m}$ = maximum vitrinite reflectance under oil immersion; Mad = moisture content (wt. %, air dry basis); Aad = ash yield (wt. %,

485   air dry basis); Vad = volatile matter (wt. %, air dry basis); FCad = fixed carbon (wt. %, air dry basis).

486

487

488

489

490

491

492

493

494

495

496

497

498

499

500

501

502

503

504

505

506

507

508

509

510

511

512

513

514

515

516

517

518

519

520

521

522

523   Table 2 The average structural parameters of open fractures and mineral-filled fractures in sample FK and ML.

Sample no.	Structural parameter	Fracture type		
		Open fractures	Mineral-filled fractures	Total fractures
FK	AL（μm）	67.55	81.56	76.80
	AW（μm）	4.83	5.10	5.05
	AA（μm^2）	5.23×10^4	1.00×10^5	8.91×10^4
	AV（μm^3）	2.16×10^5	1.33×10^6	1.07×10^6
ML	AL（μm）	58.82	934.30	67.87
	AW（μm）	2.48	26.21	2.73
	AA（μm^2）	2.20×10^4	5.57×10^6	7.93×10^4
	AV（μm^3）	4.46×10^4	4.03×10^7	4.61×10^5

524   Notes: AL=average length; AW=average width; AA=average area; AV=average volume.

525
526
527
528
529
530
531
532
533
534
535
536
537
538
539
540
541
542
543
544
545
546
547
548
549
550
551
552
553
554
555

556   Table 3 Comparison of structural parameters between open fractures and total fractures, sample FK and ML.

Relative growth rate between OAT（%）	Sample no.		Relative decline rate between FAM（%）	Fracture type	
	FK	ML		Open fracture	Total fracture
AL	15.84	15.39	AL	12.92	13.27
AW	4.46	9.87	AW	48.74	45.94
AA	67.69	261.39	AA	58.71	11.01
AV	390.07	933.39	AV	79.51	56.78

557   Notes: AL=average length; AW=average width; AA=average area; AV=average volume; OAT=open fractures and total fractures;

558   FAM=FK and ML sample.